The final publication is available at

https://doi.org/10.1016/j.cattod.2017.05.001

Additional Information

# The impact of support surface area on the SMSI decoration effect and catalytic performance for Fischer-Tropsch synthesis of Co-Ru/TiO$_2$-anatase catalysts

**Francine Bertella[a,b], Patrícia Concepción[a], Agustín Martínez[a,*]**

[a] *Instituto de Tecnología Química, Universitat Politècnica de València - Consejo Superior de Investigaciones Científicas (UPV-CSIC), Avda. de los Naranjos s/n, 46022 Valencia, Spain*

[b] *CAPES Foundation, Ministry of Education of Brazil, 70040-020 Brasilia-DF, Brazil*

* Corresponding author: amart@itq.upv.es (A. Martínez)

**Abstract**

A series of Co-Ru/TiO$_2$ catalysts (10 wt% Co, 0.5 wt% Ru, nominal loadings) were prepared by impregnation of TiO$_2$-anatase supports synthesized with different specific surface areas (Ti-L: 53 m$^2$/g, Ti-M: 117 m$^2$/g, and Ti-H: 148 m$^2$/g) by tuning the conditions of the hydrothermal synthesis and/or the calcination treatments. The most relevant physicochemical properties of supports and catalysts were determined by a set of techniques including ICP-OES, XRD, N$_2$ physisorption, electron microscopy (FESEM, HAADF-STEM, HR-TEM), H$_2$-TPR, H$_2$ chemisorption, and IR-CO. Oxidized precursors were reduced in-reactor under flowing pure H$_2$ at 400 °C for 10 h and evaluated for Fischer-Tropsch synthesis (FTS) in a fixed bed reactor at 220 °C, 2.0 MPa, and H$_2$/CO molar ratio of 2. These catalysts exhibited the well-known strong metal-support interaction (SMSI) effect reported for TiO$_2$ materials by which partially reduced TiO$_x$ species formed during the catalyst reduction step migrate and decorate the surface of the supported metal phases. The extent to which the SMSI effect occurred was found to increase proportionally to the surface area of the TiO$_2$-anatase carrier, as supported by H$_2$ chemisorption, TEM, and IR-CO surface titration experiments. As a consequence, the activity per total mass of cobalt or cobalt-time-yield (CTY) of the Co-Ru/TiO$_2$ catalysts gradually declined with the increase in support surface area: Co-Ru/Ti-L > Co-Ru/Ti-M > Co-Ru/Ti-H. The catalysts, however, displayed similar initial TOFs, implying a negligible influence of the SMSI effect on the initial intrinsic activity of the surface Co$^0$ sites. The high surface area Co-Ru/Ti-H catalyst exhibiting the most pronounced SMSI also presented the lowest C$_{5+}$ selectivity. This behavior was explained by considering the contribution of two effects: the lower resistance to the intraparticle diffusion of α-olefins when increasing the support surface area, as inferred from the olefin-to-paraffin ratios and the values of the diffusion-related parameter $\chi$, and the reduction in size of the cobalt ensembles on the terraces of Co$^0$ nanoparticles, connected to the extent of SMSI, on which chain growth events are favored.

*Keywords*: Fischer-Tropsch synthesis; cobalt catalyst; TiO$_2$-anatase; strong metal-support interaction; support surface area.

# 1. Introduction

Cobalt catalysts supported on porous metal oxides (e.g. $SiO_2$, $Al_2O_3$, and $TiO_2$) are commercially employed in Fischer-Tropsch synthesis (FTS) processes to produce high-performance clean-burning fuels, particularly diesel, from fossil carbon sources alternative to oil such as natural gas and coal as well as, more recently, from renewable biomass via the intermediate synthesis of *syngas* (mixture of CO and $H_2$) [1,2]. The catalytic performance of Co-based FTS catalysts under industrially-relevant conditions is determined by the combination of multiple parameters among which the dispersion (i.e. particle size) and distribution of the metallic cobalt nanoparticles on the support surface [3-5], the texture, morphology, and chemical nature of the support [6-8], the presence of metal and/or metal oxide promoters [9-12], and the so-called thermal history (the conditions of the thermal treatments given to the catalyst prior to FTS) [13] are probably the most influencing ones. A strong dependence of the intrinsic activity (turnover frequency or TOF) for FTS on $Co^0$ particle size by which the TOF drastically decreases below a critical size of 6-9 nm (depending on catalyst and reaction conditions) has been unequivocally reported for model cobalt catalysts supported on weakly interacting materials, favoring the reduction of small cobalt nanoparticles, such as carbon nanofibers [3] and surface-silylated pure silica ITQ-2 zeolite [4]. For more interacting supports like $Al_2O_3$ and $TiO_2$, however, discrepancies regarding the $Co^0$ particle size-TOF dependence can be the found in earlier works [14-16] which probably arise from to the difficulty to prepare appropriate model catalysts with narrow cobalt particle size distribution and high reducibility in the size range of interest (< 10 nm). On the other hand, the porous structure of the support is known to affect the FTS performance by influencing the metal dispersion [6] and the transport rate of CO and products (i.e. $\alpha$-olefins) through the catalyst pores under industrially-relevant conditions [17].

Among the main supports employed in the preparation of industrial Co-based catalysts, $TiO_2$ is particularly attractive from the viewpoint of both activity and selectivity to the targeted liquid ($C_{5+}$) hydrocarbons [18]. Nonetheless, in spite of their obvious interest, $TiO_2$-supported cobalt catalysts have been less investigated than those comprising $SiO_2$ or $Al_2O_3$. This can be probably ascribed to a higher complexity of the $Co/TiO_2$ systems that originates from the particular features of titania exhibiting different crystallographic polymorphs (anatase, rutile, brookite) and the well known strong metal-support interaction

(SMSI) effect by which partially reduced $TiO_x$ species generated during the reduction treatment migrate and decorate the surface of the supported metal nanoparticles inhibiting their CO and $H_2$ chemisorption capacity. In a recent study, we demonstrated that Ru-promoted cobalt catalysts supported on pure $TiO_2$-anatase experienced a more pronounced SMSI effect and, in consequence, a decreased cobalt-mass-based activity during FTS in comparison to those supported on pure $TiO_2$-rutile [19]. Besides crystalline phase and phase composition, other $TiO_2$ properties might also affect the SMSI effect and, hence, the catalytic behavior of $TiO_2$-supported catalysts. To this respect, Abdel-Mageed et al. [20] have recently observed an enhanced SMSI decoration effect when increasing the surface area of $TiO_2$ in Ru/$TiO_2$ catalysts. The decrease in the concentration of surface metallic Ru sites resulting from the more pronounced SMSI effect overcompensated the higher metal dispersion of the catalyts based on $TiO_2$ with higher surface areas producing a decrease in the overall catalytic activity for selective CO methanation in $CO_2$-rich reformate gases [20]. Similarly, Bonne et al. [21] observed a higher SMSI effect in Pt/$TiO_2$-$SiO_2$ nanocomposites comprising small $TiO_2$ crystallites compared to a conventional Pt/$TiO_2$ (P25) catalyst, and proposed tuning the $TiO_2$ crystal size (by varying the $TiO_2$ content in the nanocomposites) as an effective means of controlling the SMSI effect. However, none of these works provided a rationale for the observed variation in the SMSI extent with the crystallite size (i.e. surface area) of the $TiO_2$ carrier.

According to the previous discussions, we here investigated the impact of the surface area of 100% pure $TiO_2$-anatase supports on the extent of SMSI and the catalytic performance of Ru-promoted Co/$TiO_2$ catalysts for Fischer-Tropsch synthesis at typical reaction conditions of 220 °C, 2.0 MPa, and $H_2$/CO molar ratio of 2.

## 2. Experimental

### 2.1. Synthesis of TiO₂-anatase supports

Pure $TiO_2$-anatase supports with different surface areas were synthesized by a hydrothermal method using titanium(IV) *n*-butoxide (99+%, Alfa Aesar) as titanium source and acetic acid (99.5%, Aldrich). Briefly, titanium(IV) *n*-butoxide was added dropwise to an acetic acid solution under magnetic stirring at room temperature. Subsequently, the mixture was introduced into a Teflon-lined stainless steel autoclave and hydrothermally treated at selected temperatures for 24 h. Afterwards, the solid was recovered by centrifugation,

washed 5 times with ethanol in a process involving redispersion and centrifugation, dried at 60°C overnight, and finally calcined. In this way, three $TiO_2$-anatase samples with surface areas ranging from 53 to 148 $m^2$/g were obtained by varying the concentration of the acetic acid solution, the synthesis temperature, and the calcination conditions, as summarized in Table 1. The $TiO_2$-anatase supports with high, medium, and low surface area were labeled as Ti-H, Ti-M, and Ti-L, respectively. As seen in Table 1, samples with lower surface area were obtained by using higher acetic acid concentrations, higher synthesis temperatures, and by applying higher temperatures, static conditions, and higher heating rates during the final calcination step.

**Table 1.** Nomenclature and conditions employed for the hydrothermal synthesis of pure $TiO_2$-anatase with different specific surface areas.

| Support | Acetic acid | | Synthesis temperature (°C) | Calcination | | |
| | Concentration (mol/L) | Volume (mL) | | T (°C) | Air condition[a] | Heating rate (°C/min) |
| --- | --- | --- | --- | --- | --- | --- |
| Ti-H | 1.5 | 28 | 120 | 400 | Air flow | 1 |
| Ti-M | 10 | 20 | 150 | 400 | Static air[a] | 5 |
| Ti-L | Pure (P.A.) | 20 | 200 | 500 | Static air[a] | 5 |

[a] Calcined in a muffle furnace.

### 2.2. Synthesis of Co-Ru/TiO₂ catalysts

Co-Ru/$TiO_2$ catalysts were prepared by incipient wetness co-impregnation of the calcined $TiO_2$ supports with an aqueous solution containing the required amounts of $Co(NO_3)_2.6H_2O$ (Aldrich) and ruthenium(III) nitrosyl nitrate (Aldrich) precursors to achieve a nominal composition of 10 wt% Co and 0.5 wt% Ru. Next, the catalysts were dried at 100 °C overnight and calcined in flowing air at 300 °C for 3 h. The catalysts supported on high, medium, and low surface area $TiO_2$-anatase were labeled as Co-Ru/Ti-H, Co-Ru/Ti-M, and Co-Ru/Ti-L, respectively.

### 2.3. Characterization techniques

Chemical compositions were obtained by Inductively Coupled Plasma-Optical Emission Spectrometry (ICP-OES) in a Varian 715-ES spectrometer after digestion of the solids in an acid mixture of $HNO_3$:HF:HCl (1:1:3 volume ratio).

X-ray powder diffraction (XRD) patterns were recorded on a Philips X'Pert diffractometer using monochromatized Cu-K$_\alpha$ radiation ($\lambda$ = 0.15406 nm). The average diameter of the $TiO_2$ crystallites were obtained by line broadening analysis applied to the most intense (1 0 1) reflection of anatase ($2\theta$ = 25.28°) using the Scherrer's equation and assuming a shape factor k = 0.9.

The $N_2$ adsorption isotherms were measured at -196 °C in a Micromeritics ASAP-2420 equipment after degassing the samples at 300 °C under vacuum overnight. Specific surface areas were obtained following the Brunauer-Emmett-Teller (BET) method, total pore volumes were determined at a relative pressure of 0.98, and pore size distributions were derived by applying the Barrett-Joyner-Halenda (BJH) approach to the adsorption branch of the isotherms.

The morphology of the samples were studied by field emission scanning electron microscopy (FESEM) using a ZEISS Ultra-55 microscope.

Raman spectra for the pristine high surface area (Ti-H) and low surface area (Ti-L) anatase-$TiO_2$ samples and after reduction in flowing $H_2$ at 400°C for 10 h were acquired in a Renishaw in Via Raman spectrometer equipped with a Leica DMLM microscope. A 50x objective of 1 mm optical length was used to focus the depolarized laser beam onto a 3–5 µm spot on the sample surface and collect the backscattered light. As an excitation source a 514 nm HPNIR diode laser was used and the laser power at the sample was 25 mW. The Raman scattering was collected in a static-scan mode in the 100-800 cm$^{-1}$ spectral region with resolution > 4 cm$^{-1}$.

Reduction profiles for the Co-Ru/$TiO_2$ catalysts were measured by hydrogen temperature-programmed reduction ($H_2$-TPR) in a Micromeritics Autochem 2910 device. The samples (ca. 100 mg) were flushed with an Ar flow at room temperature for 30 min, and then the gas was switched to a gas mixture of $H_2$ diluted (10 vol%) in Ar. Next, the temperature was linearly increased up to 900 °C at a heating rate of 10 °C/min while monitoring the $H_2$ consumption in a thermal conductivity detector (TCD) pre-calibrated using the reduction of a standard CuO sample as reference. Water generated during the reduction was retained in a 2-propanol/$N_{2(liq)}$ trap located downstream the analyzer to ensure that only

$H_2$ is detected in the TCD. Additional experiments were performed in the same equipment in order to determine the degree of cobalt reduction (DR). To this purpose, the catalysts were first reduced in pure flowing $H_2$ at 400 °C for 10 h (the same conditions applied prior to the FTS reactions). Then, the gas was switched to the diluted $H_2$ stream (10 vol% $H_2$ in Ar) and the temperature increased from 400 °C to 800 °C at a rate of 10 °C/min while registering the signal of $H_2$ in the TCD. DR values were calculated assuming that the $H_2$ consumed in this last step corresponds to the reduction of cobalt oxide (in the form of CoO) remaining after the 400 °C reduction treatment.

Cobalt dispersions were determined by $H_2$ chemisorption at 100 °C in an ASAP 2010C Micromeritics equipment by extrapolating the total gas uptakes in the adsorption isotherms at zero pressure [18]. Prior to the measurements the samples (about 300 mg) were reduced under flowing pure $H_2$ at 400 °C for 10 h. Metal particle sizes ($d(Co^0)_{H2}$) were estimated from the total amount of chemisorbed $H_2$, assuming an adsorption stoichiometry H/Co of 1, the Co content (from ICP-OES), the degree of cobalt reduction, and considering spherical particle geometry with a surface atomic density of 14.6 atoms/nm$^2$.

Cobalt particle sizes were also determined by transmission electron microscopy in a JEOL-JEM-2100 F microscope operating at 200 kV in scanning transmission mode (STEM) using a High-Angle Annular Dark Field (HAADF) detector. Before microscopy observation, the samples were prepared by suspending the solid in dichloromethane and submitting the suspension to ultrasonication for one minute. Afterwards, the suspension was let to slowly decant for two minutes and a drop was extracted from the top side and placed on a carbon-coated copper grid. The catalysts were previously reduced ex situ under a flow of $H_2$ at 400 °C, passivated at r.t. under a flow of 0.5 vol% $O_2/N_2$ and stored at r.t. until the sample preparation for microscopy. Metal particle size histograms were generated upon measurement of 150–200 particles from several micrographs taken at different positions on the TEM grid. Average cobalt particle sizes ($d(Co^0)_{TEM}$) were corrected for a 2.5 nm thick CoO passivation outlayer as measured by high-resolution transmission electron microscopy (HR-TEM).

IR-CO spectra were recorded with a Nexus 8700 FTIR spectrometer using a DTGS detector and acquiring at 4 cm$^{-1}$ resolution. An IR cell allowing in situ treatments in controlled atmospheres and temperatures in the 25-500 °C range was connected to a vacuum system with gas dosing facility. For IR studies, the samples (pre-reduced ex situ at

400 °C for 10 h in pure $H_2$ flow and subsequently passivated) were pressed into self-supported wafers of 10 mg/cm$^2$, reduced again in the cell at 400 °C for 2 h in flowing $H_2$, and submitted to a vacuum treatment at 450 °C for 1 h. Afterwards, the samples were cooled down to 25 °C under dynamic vacuum and CO was then dosed at increasing pressures (1.9-30 mbar). IR spectra were recorded after each dosage. Spectra analysis was done using the Origin software.

### 2.4. Fischer-Tropsch synthesis experiments

Catalytic experiments were performed in a down-flow fixed-bed stainless steel reactor with internal diameter of 10 mm and length of 40 cm. The reactor was loaded with 0.5 g of catalyst (0.25-0.42 mm pellet size) diluted with SiC granules (0.6-0.8 mm) until a total bed volume of 6.4 cm$^3$. Prior to reaction, the catalysts were reduced in situ in flowing $H_2$ at 400 °C for 10 h at ambient pressure. After reduction, the temperature was decreased to 100 °C under flowing $H_2$ and then *syngas* with $H_2$/CO molar ratio of 2 (CO:$H_2$:Ar volume ratio of 3:6:1, Ar used as internal standard for GC analyses) was passed through the reactor at the desired flow rate, the reaction pressure increased up to 2.0 MPa, and the temperature raised up to 220 °C at a rate of 2 °C/min. The temperature in the catalytic bed was controlled by two thermocouples connected to independent PID controllers. A third vertically sliding thermocouple was used to verify the absence of temperature gradients (T = 220 ± 1 °C) after the reaction temperature was established. Initial FTS activities were determined at quasi-differential CO conversions (<10%) using a constant gas hourly space velocity (GHSV) of 11.7 $L_{syngas}$/($g_{cat}$·h) to ensure a low water partial pressure in the catalytic bed. This condition was maintained during ca. 7-8 h on stream, after which the GHSV was adjusted for each catalyst so as to achieve a constant CO conversion of 10 ± 2% in the *pseudo*-steady state. Heavier hydrocarbons and water were condensed in two consecutive traps located at the reactor outlet and kept, respectively, at 150 °C and 100 °C, both at the reaction pressure (2.0 MPa). The stream leaving the second trap was depressurized and regularly analyzed on line by gas chromatography (GC) in a Varian 450 chromatograph equipped with three columns and TCD and FID detectors. After separation of the water co-product, the hydrocarbon fractions collected in the traps were weighted, diluted with $CS_2$, and analyzed off line in the same GC. The combination of the on line and off line GC analyses through the common product

methane resulted in carbon mass balances in the 98-102% range. Product selectivities are expressed on a carbon basis.

## 3. Results and Discussion

### 3.1. Characterization of TiO₂-anatase supports

The XRD patterns of the calcined supports (Fig. 1) confirm that anatase (JCPDS 00-021-1272) is the only crystalline $TiO_2$ phase in all three synthesized supports. It is known from previous studies that the crystallization as anatase or rutile polymorphs is closely related to the type of acid used during the synthesis [22,23]. In the presence of acetic acid, as applied in this work, the $CH_3COO^-$ anions coordinate strongly to titanium preventing the transformation of the metastable anatase to the thermodynamically favored rutile phase [22,24]. The XRD-derived mean particle sizes for the calcined $TiO_2$-anatase materials are shown in Table 2. As previously commented, materials with larger $TiO_2$ particle size could be obtained by using higher temperatures and acetic acid concentrations during the hydrothermal syntheses as well as more severe calcination conditions. Hence, the mean $TiO_2$ particle size increased from 11 nm for Ti-H to 14 nm for Ti-M and further to 27 nm for Ti-L.
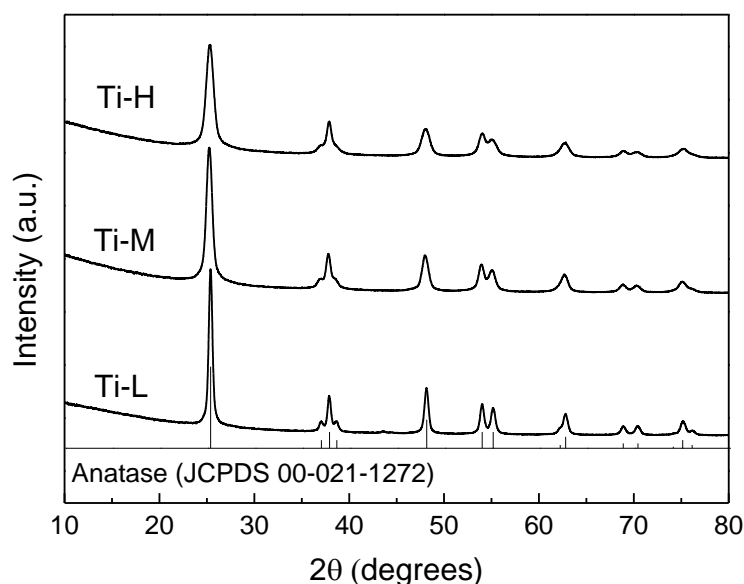


**Fig. 1.** X-ray diffraction patterns of calcined $TiO_2$ supports exhibiting the characteristic diffraction peaks of the anatase phase (JCPDS 00-021-1272).

The N$_2$ adsorption-desorption isotherms and corresponding pore size distributions for calcined TiO$_2$ samples are shown in Fig. 2, and the derived textural properties are gathered in Table 2. All TiO$_2$ supports present type IV adsorption isotherms (Fig. 2a) characteristic of mesoporous solids with a large hysteresis loop at high relative pressure related to capillary condensation [25], similar to those previously reported for mesoporous TiO$_2$ synthesized using triblock copolymers as mesoporogens [26,27]. It is worth noting that in spite of having used distinct acid concentrations and temperatures in the syntheses, the type of pores, as indicated by the shape of the hysteresis loop, is similar for all three TiO$_2$-anatase samples. According to the N$_2$ uptakes, the BET areas follow, as expected, the reverse trend of TiO$_2$ particle sizes, decreasing from 148 m$^2$/g for Ti-H to 53 m$^2$/g for Ti-L, with Ti-M presenting an intermediate BET value of 117 m$^2$/g (Table 2). Moreover, all TiO$_2$ supports display unimodal pore size distributions with maxima at 8.8, 11.7, and 11.8 nm for Ti-H, Ti-M, and Ti-L, respectively (Fig. 2b). Note, however, that the sample with medium surface area, Ti-M, exhibits a broader distribution of pore sizes in comparison to Ti-H and Ti-L. Nevertheless, the average pore diameter follows an opposite trend to the specific surface areas, progressively increasing from 6.1 to 8.4 nm with decreasing the BET area of the TiO$_2$-anatase material from 148 to 53 m$^2$/g (Table 2). In turn, it can be seen in Table 2 that the Ti-L sample with the lowest surface area also presents the lowest total pore volume (0.13 cm$^3$/g), while both Ti-H and Ti-M samples show higher and alike total pore volumes (0.26 $\pm$ 0.01 cm$^3$/g).
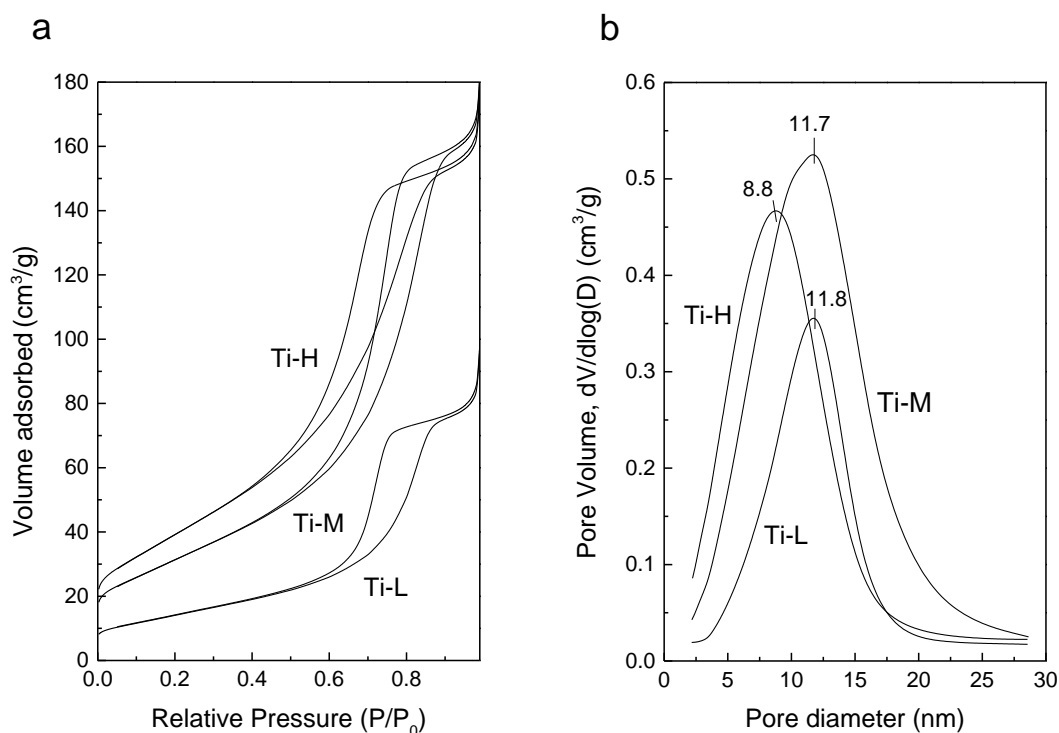
**Fig. 2.** N$_2$ adsorption-desorption isotherms (a) and corresponding pore size distributions (b) for calcined TiO$_2$-anatase carriers.

**Table 2.** TiO$_2$ particle size (XRD) and textural properties of TiO$_2$-anatase supports derived from N$_2$ physisorption.

| Support | TiO$_2$ particle size (nm) | BET area (m$^2$/g) | Total pore volume (cm$^3$/g) | Average pore diameter (nm) |
|---------|----------------------------|--------------------|------------------------------|----------------------------|
| Ti-H | 11 | 148 | 0.25 | 6.1 |
| Ti-M | 14 | 117 | 0.27 | 7.8 |
| Ti-L | 27 | 53 | 0.13 | 8.4 |

Differences in particle size among the prepared TiO$_2$ supports were also clearly perceived by electron microscopy, as seen in the representative FESEM images shown in Fig. 3. In all cases agglomerated particles comprised of small rice-like crystallites of distinct sizes were found, indicating that the morphology of the TiO$_2$ crystallites becomes mainly dictated by the nature of the acid employed in the synthesis, in agreement with earlier observations [22]. The size of the crystallites, however, evidently increased with the decrease of the specific surface area, ranging 10-30 nm for Ti-H, 15-35 nm for Ti-M, and 20-50 nm for Ti-L.
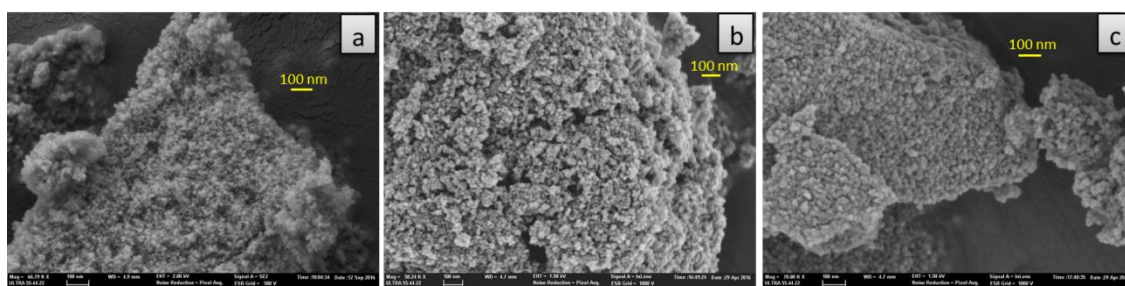
**Fig. 3.** Representative FESEM images for calcined TiO$_2$-anatase supports: Ti-H (a), Ti-M (b), and Ti-L (c).

### 3.2. Characterization of Co-Ru/TiO$_2$ catalysts

The XRD patterns of the Co-Ru/TiO$_2$ catalysts in their oxidized state are presented in Fig. 4. Peaks corresponding to the Co$_3$O$_4$ spinel phase (JCPDS 00-042-1467) were detected for all three samples besides the characteristic reflections of the TiO$_2$-anatase phase. No additional crystalline phases related to cobalt or TiO$_2$ were perceived. Moreover, line broadening analysis of the TiO$_2$ peaks indicated no practical differences in the mean TiO$_2$ particle size between the catalysts and the corresponding supports. An accurate estimation of the Co$_3$O$_4$ mean particle size was, however, not feasible due to the relative low intensity of the Co$_3$O$_4$ spinel reflections and overlapping with TiO$_2$ diffractions.
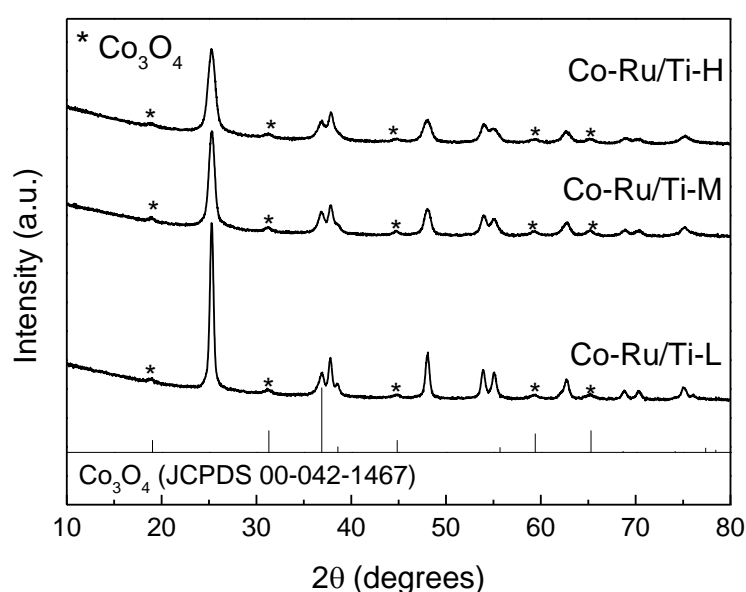
**Fig. 4.** X-ray diffraction patterns of calcined Co-Ru/TiO$_2$ catalysts. The characteristic diffraction lines of Co$_3$O$_4$ spinel (JCPDS 00-042-1467) are also shown for an easier visualization of the Co$_3$O$_4$-related diffractions in the catalysts.

As observed in Fig. 5a, the calcined Co-Ru/TiO$_2$ catalysts exhibit type IV N$_2$ adsorption-desorption isotherms characteristic of mesoporous solids similar to those of the corresponding supports. The BJH pore size distributions (Fig. 5b) are, also, alike to the TiO$_2$ supports, with maxima at 10.6, 11.8, and 9.5 nm for Co-Ru/Ti-L, Co-Ru/Ti-M, and Co-Ru/Ti-H, respectively. The derived textural properties are given in Table 3. The BET surface area and total pore volume of the catalysts decreased by about 15-25% with respect to the values of the corresponding supports. This reduction is mostly ascribed to the dilution effect caused by the presence of the metal oxide phases. Indeed, BET areas and total pore volumes recalculated per mass of support (Table 3) are only less than 7% lower than those of the carriers (Table 2), indicating negligible pore blockage by the supported metal oxides. This is more evident for the catalyst based on the low surface area Ti-L sample comprising larger mesopores, for which the values of BET area and total pore volume recalculated per mass of TiO$_2$ are identical to those of the bare support. Moreover, the average pore diameters of the catalysts (Table 3) do not show significant variations with respect to those of the pristine carriers.
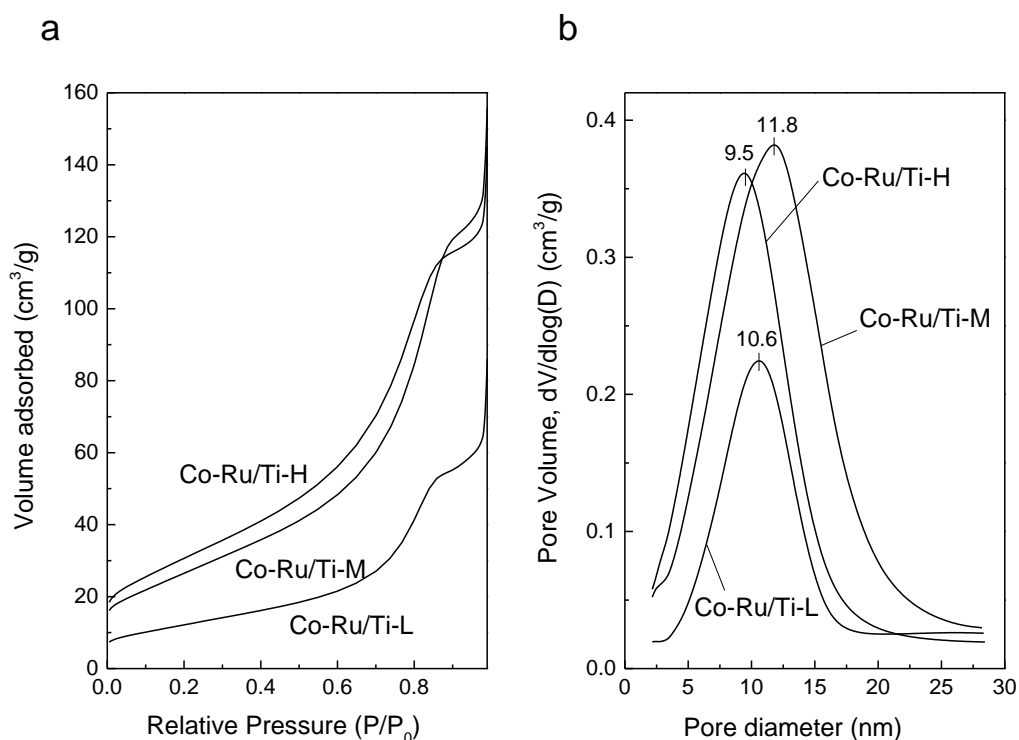
**Fig. 5.** $N_2$ adsorption isotherms (a) and pore size distributions (b) for calcined Co-Ru/TiO$_2$ catalysts.

**Table 3.** Chemical composition and textural properties of calcined Co-Ru/TiO$_2$ catalysts.

| Catalyst | Metal content (wt%) | | BET area[a] ($m^2$/g) | Total pore volume[a] ($cm^3$/g) | Average pore diameter (nm) |
|---|---|---|---|---|---|
| | Co | Ru | | | |
| Co-Ru/Ti-H | 11.8 | 0.2 | 113 (135) | 0.20 (0.24) | 6.4 |
| Co-Ru/Ti-M | 11.8 | 0.4 | 99 (118) | 0.21 (0.25) | 7.5 |
| Co-Ru/Ti-L | 11.1 | 0.2 | 45 (53) | 0.11 (0.13) | 7.9 |

[a] Data in parentheses correspond to the values recalculated per mass of TiO$_2$ support.

The Co and Ru contents measured by ICP-OES are presented in Table 3. The concentration of cobalt slightly exceeds the targeted value (10 wt%) by about 10%. However, ruthenium contents are notably lower (by 20-60%) than the nominal content (0.5 wt%) due the formation of volatile sub-oxide RuO$_x$ species during calcination under oxidizing atmosphere [28].

The reducibility of the Co-Ru/TiO$_2$ catalysts was studied by H$_2$-TPR and the corresponding reduction profiles are presented in Fig. 6. All catalysts display two main reduction features with maximum H$_2$ consumptions at temperatures of ca. 125-170 °C (T1$_{max}$) and ca. 275-320 °C (T2$_{max}$). The low-temperature and high-temperature reduction features are ascribed, respectively, to the well-known two-step reduction of Co$_3$O$_4$ to Co$^0$ (T1: Co$_3$O$_4$ → CoO; T2: CoO → Co$^0$). The broad temperature range of the T2$_{max}$ reduction peak signs for the presence of CoO with different degrees of interaction with the TiO$_2$ support [29]. Additionally, a relatively small reduction feature at higher temperatures (T3$_{max}$= 392-425 °C) is perceived for the three catalysts, indicative of Co$^{2+}$ species displaying a stronger interaction with the TiO$_2$ carrier. It is worth noting that the maximum temperatures for these three reduction peaks gradually shift towards higher values when decreasing the surface area of the TiO$_2$-anatase support (Fig. 6). This trend could be related to an increasing mean size of the Co$^0$ nanoparticles with the decrease in support surface area, as will be discussed next based on TEM data. Previous studies did also found higher reduction temperatures for larger cobalt nanoparticles in Co/TiO$_2$ catalysts [30]. Nonetheless, at the view of the obtained H$_2$-TPR profiles, a high extent of cobalt reduction might be inferred for all three Co-Ru/TiO$_2$ catalysts upon reduction in pure H$_2$ at 400 °C for 10 h, as performed prior to catalysis. This is confirmed by the high (and similar) degrees of cobalt reduction (87-91%) obtained in the additional H$_2$-TPR experiments on pre-reduced catalysts, as seen in Table 4. The high degrees of cobalt reduction achieved are attributable to the presence of Ru in the catalysts and its well known role as reduction promoter [9,28,31]. Moreover, in situ H$_2$-XRD measurements did not reveal diffractions related to cobalt oxide (Co$_3$O$_4$ and/or CoO) phases upon reducing the catalysts in flowing H$_2$ at 400°C, supporting the high degree of cobalt reduction concluded from the H$_2$-TPR experiments (see Figure S1 in Supplementary Material). Conversely, the H$_2$-XRD results indicated the coexistence of both *fcc*-Co$^0$ (JCPDS 00-15-0806) and *hcp*-Co$^0$ (JCPDS 00-005-0727) crystalline phases in the reduced catalysts (Figure S1).
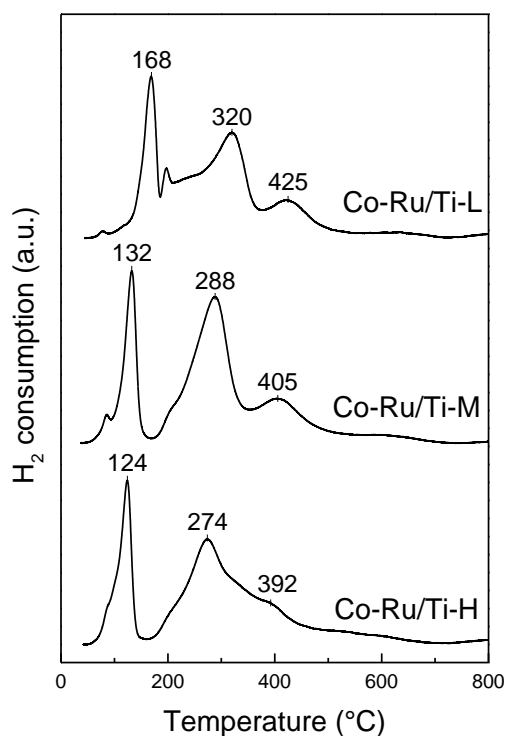
**Fig. 6.** H$_2$-TPR profiles for Co-Ru/TiO$_2$ catalysts.

Table 4 summarizes the main properties of cobalt in the Co-Ru/TiO$_2$ catalysts. Hydrogen chemisorption experiments revealed increasing H$_2$ uptakes with decreasing the TiO$_2$ surface area, going from 17.6 µmol/g$_{cat}$ for Co-Ru/Ti-H to 24.5 µmol/g$_{cat}$ for Co-Ru/Ti-L. Such H$_2$ uptakes translate into apparent cobalt particle sizes (d(Co$^0$)$_{H2}$ in Table 4) of 48.2 nm for Co-Ru/Ti-H, 39.5 nm for Co-Ru/Ti-M, and 33.7 nm for Co-Ru/Ti-L.

**Table 4.** Properties of cobalt in the Co-Ru/TiO$_2$ catalysts.

| Catalyst | H$_2$ uptake (µmol/g$_{cat}$) | Degree of cobalt reduction (%) | Co$^0$ particle size (nm) | | d(Co$^0$)$_{H2}$/ d(Co$^0$)$_{TEM}$ ratio |
| | | | d(Co$^0$)$_{H2}$ | d(Co$^0$)$_{TEM}$ | |
| --- | --- | --- | --- | --- | --- |
| Co-Ru/Ti-H | 17.6 | 88.3 | 48.2 | 7.2 | 6.7 |
| Co-Ru/Ti-M | 21.2 | 87.1 | 39.5 | 7.4 | 5.3 |
| Co-Ru/Ti-L | 24.5 | 91.2 | 33.7 | 9.1 | 3.7 |

Metal cobalt particle sizes were also measured by STEM after reduction in H$_2$ at 400 °C and passivation. Representative HAADF-STEM images and their corresponding particle

size histograms are shown in Fig. 7. In all Co-Ru/TiO$_2$ catalysts metallic cobalt nanoparticles, visible as bright spots in the images, appear well dispersed over the TiO$_2$-anatase supports, although some clustered regions are also evidenced, as frequently observed in catalysts prepared by impregnation with cobalt nitrate precursor [6]. It is observed in the histograms that the size of cobalt nanoparticles extends over a broader range in the low surface area Co-Ru/Ti-L catalyst (3-27 nm) in comparison to the medium and high surface area ones (3-18 nm). The particle size values presented in the histograms were previously corrected by a 2.5 nm thick CoO outlayer resulting from the passivation treatment, according to the representative HR-TEM image shown in Fig. 8 corresponding to the as-reduced and passivated Co-Ru/Ti-L sample. In the image, the Co$^0$ particle, identified by the lattice spacing of 0.19 nm related to the (1 0 1) plane of $hcp$-Co$^0$, appears covered by a 2.5 nm thick layer presenting a lattice spacing of 0.21 nm characteristic of the (2 0 0) crystallographic plane of CoO. As seen in Table 4, the corrected STEM-derived average Co$^0$ particle sizes, d(Co$^0$)$_{TEM}$, present an inverse relationship with the support surface area, with values of 7.2, 7.4, and 9.1 nm for Co-Ru/Ti-H, Co-Ru/Ti-M, and Co-Ru/Ti-L, respectively.
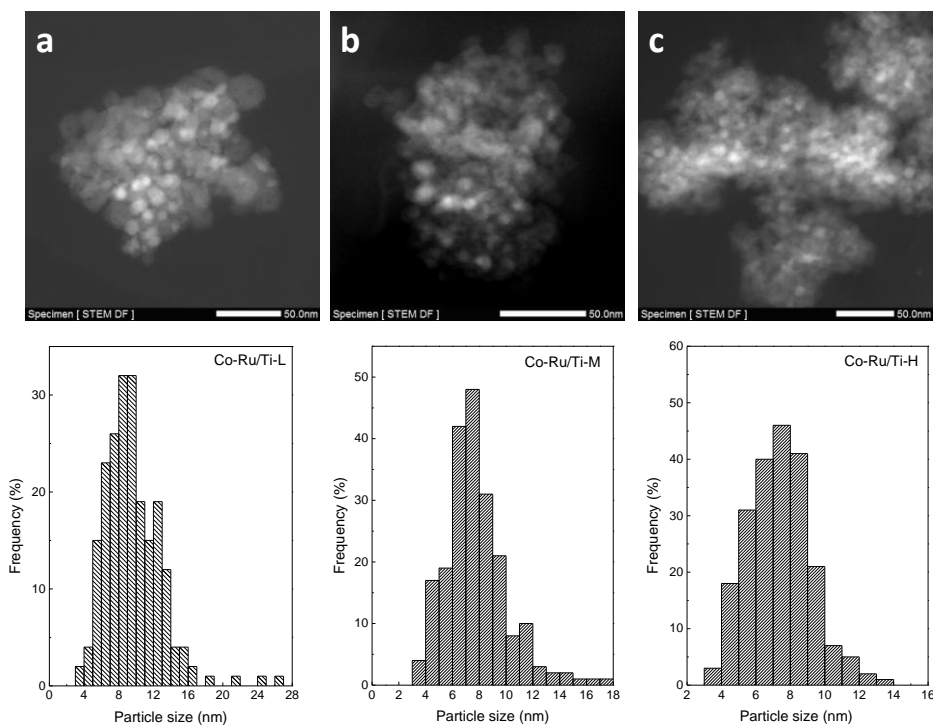
**Fig. 7.** HAADF-STEM micrographs (top) for $H_2$-reduced and passivated Co-Ru/Ti-L (a), Co-Ru/Ti-M (b), and Co-Ru/Ti-H (c) catalysts. The respective $Co^0$ particle size histograms are shown at the bottom of each image.
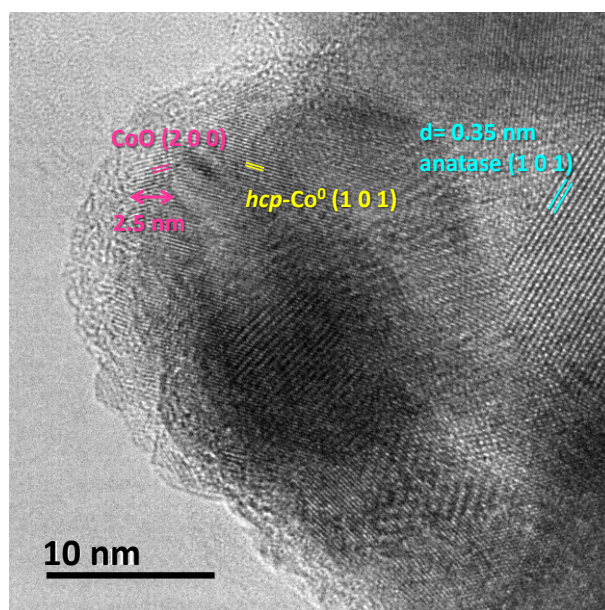


**Fig. 8.** HR-TEM micrograph of reduced and passivated Co-Ru/Ti-L catalyst showing the 2.5 nm thick CoO layer covering the surface of $Co^0$ nanoparticles.

The $Co^0$ particle sizes obtained by $H_2$ chemisorption are 3-7 times larger than those measured by direct imaging (Table 4). This apparent discrepancy is related to the SMSI effect which takes place during the reduction stage of activation where partially reduced $TiO_x$ species migrate on top of the $Co^0$ nanoparticles suppressing their $H_2$ (and CO) chemisorption capacity [32]. The ratio between the $Co^0$ particle size obtained by $H_2$ chemisorption and by direct observation (STEM), $d(Co^0)_{H2}/ d(Co^0)_{TEM}$, can be taken as an indirect estimation of the extent to which the SMSI effect occurred on the different catalysts. As shown in Table 4, this ratio increases from 3.7 for Co-Ru/Ti-L to 6.7 for Co-Ru/Ti-H, indicating that the SMSI is exacerbated by the increase in surface area of the $TiO_2$-anatase support, in line with the trends previously observed for Ru/$TiO_2$ [20] and Pt/$TiO_2$-$SiO_2$ [21] catalysts.

Finally, CO adsorption followed by IR spectroscopy has been used for identification of the amount and the nature of surface cobalt species present in the $H_2$-reduced Co-Ru/$TiO_2$

samples with extreme surface areas. The IR spectra of CO adsorption at saturation coverage (Fig. 9) shows two bands at 2065 and 1982 $cm^{-1}$ for the high surface area Co-Ru/Ti-H sample, and a broad asymmetric band peaking at 2065 $cm^{-1}$ and a tail at lower frequency ($\sim$2014 $cm^{-1}$) for the low surface area Co-Ru/Ti-L sample. The IR band at 2065 $cm^{-1}$ corresponds to CO interacting with both *fcc* and *hcp* $Co^0$ surface sites [33], while the IR bands at lower frequency ($\sim$2014 and 1982 $cm^{-1}$) have been linked to coordinatively unsaturated cobalt sites in defects (i.e. steps, edges, and corners) of the $Co^0$ crystallites or at the interface between cobalt and the metal oxide support where CO coordinates in a *tilt* configuration [4]. In the case of $TiO_2$-supported catalysts, the low frequency IR component at 1982 $cm^{-1}$ might be associated to $Co^0$ species in contact with $TiO_x$ species characteristic of the SMSI state [19]. Thus, the IR-CO results point towards a higher amount of metal-oxide surface patches in the catalyst based on the high surface area $TiO_2$-anatase resulting in different surface cobalt topologies for catalysts experiencing distinct SMSI extents. On the other hand, the amount of cobalt species titrated by CO is about 1.9 times higher in Co-Ru/Ti-L than in Co-Ru/Ti-H, according to the respective areas of the cobalt-related IR-CO bands. This area ratio compares well with the $H_2$ uptake ratio of 1.4 obtained from $H_2$ chemisorption for these two catalysts (Table 4), thus providing further evidence for the occurrence of a more pronounced SMSI effect in the catalyst supported on the high surface area carrier.
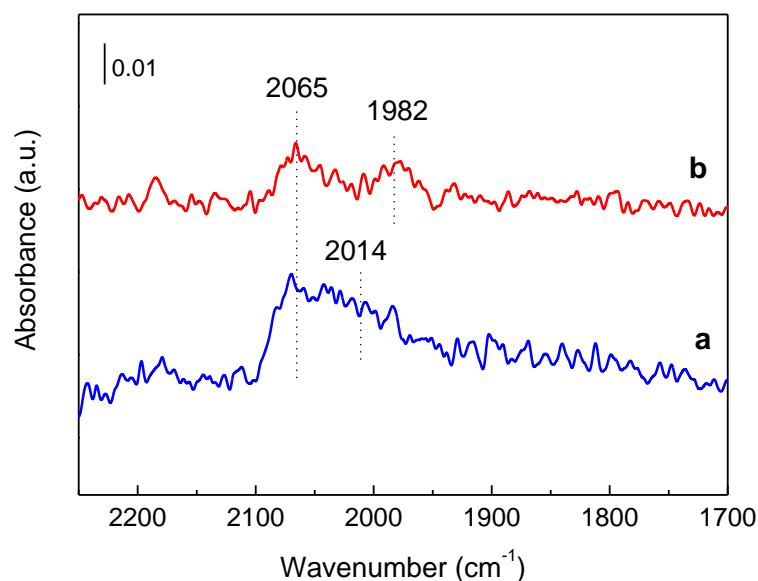
**Fig. 9.** IR spectra of CO adsorption at saturation coverage (30 mbar) for Co-Ru/Ti-L (a) and Co-Ru/Ti-H (b) catalysts after reduction in flowing $H_2$ at 400 °C.

In our earlier work, we reported an enhanced SMSI effect for Co-Ru/TiO$_2$ catalysts supported on TiO$_2$-anatase compared to those based on TiO$_2$-rutile [19]. In the present study, we have shown that, besides the crystalline phase, the TiO$_2$ surface area exerts a notable influence on the SMSI extent, with higher surface areas (i.e. lower crystallite sizes) leading to a more pronounced SMSI effect. Although the same effect has been previously reported for Ru/TiO$_2$ [20] and Pt/TiO$_2$-SiO$_2$ [21] systems, as mentioned beforehand, its genesis has not yet been clearly established. In the following, we will try to provide a rationale for the experimentally observed dependence of the SMSI extent with the TiO$_2$ surface area/crystallite size. It is known from earlier works that the SMSI state in TiO$_2$-supported metal catalysts is tightly linked to the removal of oxygen from the TiO$_2$ lattice with the consequent formation of $Ti^{3+}$/oxygen vacancy pairs during reduction in $H_2$ at high temperature [34]. Indeed, more reducible titania generally induces a larger SMSI effect [35]. On the other hand, the concentration of $Ti^{3+}$/oxygen vacancy generated upon $H_2$ reduction was shown to gradually increase with decreasing the crystallite size of the starting TiO$_2$ material [36,37], as smaller TiO$_2$ crystals are associated to more defected structures. Therefore, one may anticipate that more partially reduced $Ti^{3+}$ species, which are central to the generation of the SMSI state, would form during reduction of TiO$_2$ comprising smaller crystallites, that is, higher specific surface areas. In order to experimentally support the above hypothesis, we performed Raman spectroscopy to characterize the structural features of the high surface area (Ti-H) and low surface area (Ti-L) supports in their calcined state as well as after reduction in $H_2$ at 400°C for 10 h. The corresponding Raman spectra are shown in Figure 10a,b. As observed, the calcined Ti-H and Ti-L samples exhibit active Raman bands at ca. 146, 197, 399, 515, and 639 cm$^{-1}$ ascribed to, respectively, the E$_g$, E$_g$, B$_{1g}$, A$_{1g}$+B$_{1g}$, and E$_g$ active modes of anatase-TiO$_2$ [38]. These Raman modes, albeit with decreased intensities, are also observed for the $H_2$-reduced TiO$_2$ supports. The weakened intensity of the Raman bands originates from an enhanced nonstoichiometric property ($Ti^{3+}$/oxygen vacancy) of the $H_2$-reduced materials [36]. Specifically, the E$_g$ vibration mode is associated with planar O-O interactions and is thus sensitive to the presence of oxygen defects in the TiO$_2$ lattice. In this respect, a linear correlation has been found between the peak position and the full width at

half-maximum (FWHM) of the most intense $E_g$ mode at around 146 cm$^{-1}$ as both parameters increase with the concentration of oxygen vacancies (i.e. Ti$^{3+}$) in the TiO$_2$ lattice [39]. In agreement with this, we also observed a linear relationship between the peak position and the FWHM of this $E_g$ band for the Ti-H and Ti-L samples in their calcined and as-reduced states, as depicted in Figure 10c.
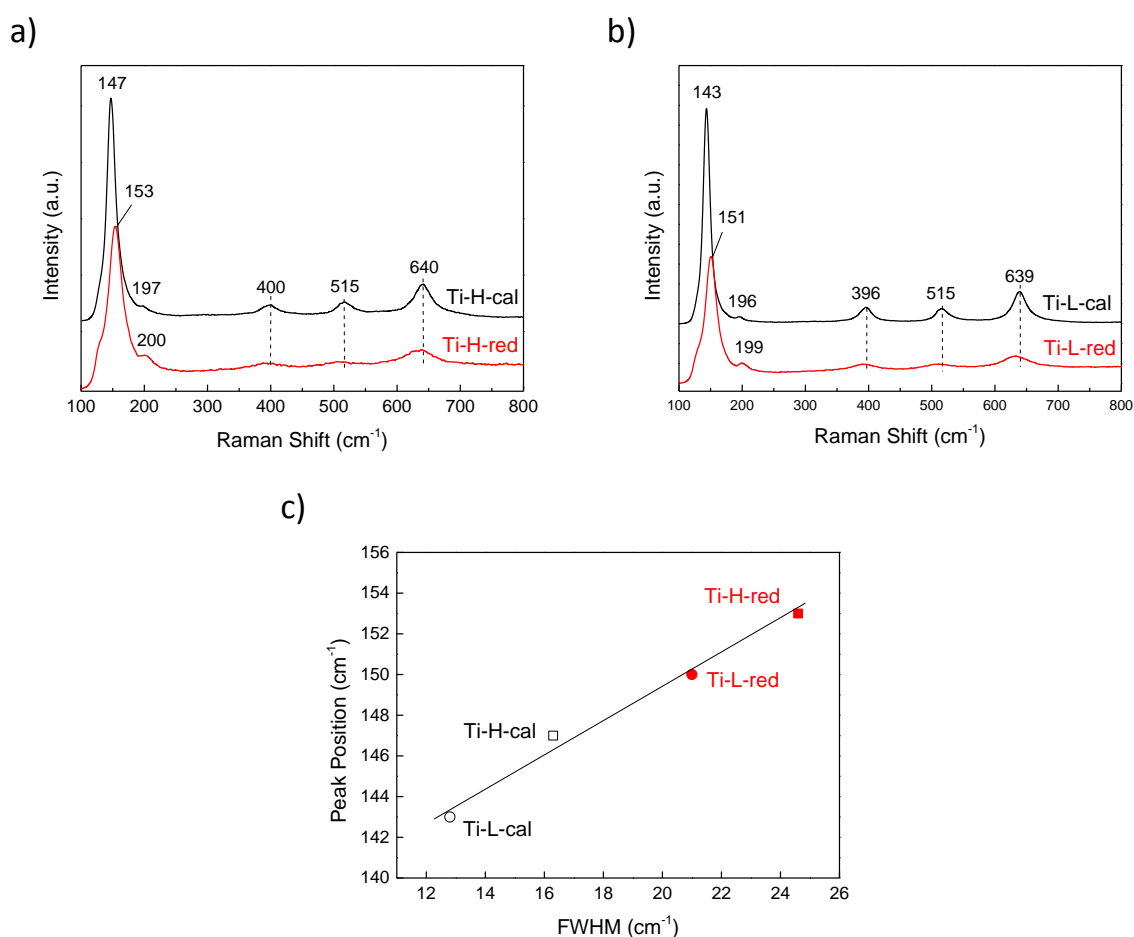


**Fig. 10**. Raman spectra for the high surface area Ti-H (a) and the low surface area Ti-L (b) anatase-TiO$_2$ supports in their calcined state ("-cal") and after reduction in H$_2$ at 400°C ("-red"); c) correlation between the peak position and the FWHM of the $E_g$ Raman band for the calcined and H$_2$-reduced Ti-H and Ti-L samples.

The trends in Figure 10c indicate an increased concentration of lattice defects in the anatase-TiO$_2$ supports upon reduction in H$_2$, as expected. Moreover, the higher wavenumber and FWHM of the $E_g$ Raman band in the high surface area Ti-H sample compared to Ti-L in both their calcined and reduced states clearly sign for a higher concentration of defects

($Ti^{3+}$/oxygen vacancy) in the former, which can be ascribed to its lower crystallite size [36,37]. According to these results, more partially reduced $TiO_x$ species would form during the reduction in $H_2$ at 400°C of the Co-Ru/$TiO_2$ catalysts with increasing the surface area (i.e. with decreasing the crystallite size) of the anatase-$TiO_2$ support resulting in a higher extension of the SMSI effect, as observed in the present study.

The consequences on the FTS reaction of the enhanced SMSI effect in high surface area Co-Ru/$TiO_2$ catalysts are analyzed in the following section.

### 3.3. Fischer-Tropsch synthesis on Co-Ru/TiO₂ catalysts

Table 5 summarizes the main catalytic properties for FTS of the investigated Co-Ru/$TiO_2$ catalysts. Initial activities were obtained by extrapolation of the conversion-time-on-stream (TOS) curves at TOS = 0 (not shown). As observed in the table, both the initial CO conversion and cobalt-time-yield (CTY) at constant GHSV progressively increased with the decrease in support surface area, with the low surface area Co-Ru/Ti-L catalyst displaying an initial activity about 1.5 times higher than the high surface area Co-Ru/Ti-H sample. The change in initial CTY with the support surface area parallels the trend in $H_2$ uptake (Table 4) and, thus, in the concentration of surface $Co^0$ sites available for reaction after $H_2$ reduction as a result of the SMSI effect. Similar trends are observed for the CTY in the *pseudo*-steady state period (at constant CO conversion of ~10%). However, the relative loss of CTY from the initial to the *pseudo*-steady state (SS) augments from 14.2% to 43.4% with the increase in support surface area (Table 5). Considering that the FTS rate of Co-based FTS catalysts displays an apparent negative kinetic dependence with respect to CO [2], this trend likely reflects the increasing resistance for the diffusion of CO through the dense hydrocarbon phase filling the catalyst pores in the *pseudo*-steady state with decreasing the support pore size [6]. Contrarily to the cobalt mass-based activity (CTY), all catalysts display nearly identical values for the initial (TOS→0) intrinsic activity per exposed $Co^0$ site (from $H_2$ chemisorption) or turnover frequency (TOF), as seen in Table 5. The obtained initial TOFs ($10\pm1\cdot10^{-2}$ $s^{-1}$) are in line with those reported for *ex*-nitrate $TiO_2$-supported Co catalysts at equivalent reaction conditions [5,7,40].

**Table 5.** Initial and *pseudo*-steady state (SS) activities of Co-Ru/TiO$_2$ catalysts for Fischer-Tropsch synthesis (FTS). Reaction conditions: T= 220 °C, P= 2.0 MPa, H$_2$/CO= 2 mol/mol. Initial activities were obtained by extrapolating the CO conversion-TOS curves at TOS= 0 at constant GHSV of 11.7 L$_{syngas}$/(g$_{cat}$·h), while SS activities were averaged for the next 8 h of reaction after adjusting the GHSV for each catalyst to obtain a CO conversion of ~10%.

| Catalyst | CO conversion (%) | | CTY·10$^3$ (mol$_{CO}$/g$_{Co}$.h)[a] | | -ΔCTY[b] | TOF·10$^2$ (s$^{-1}$)[c] | |
|---|---|---|---|---|---|---|---|
| | Initial | SS | Initial | SS | (%) | Initial | SS |
| Co-Ru/Ti-H | 7.4 | 9.3 | 100.0 | 56.6 | 43.4 | 9.3 | 5.3 |
| Co-Ru/Ti-M | 10.3 | 11.5 | 141.1 | 108.6 | 23.0 | 10.9 | 8.4 |
| Co-Ru/Ti-L | 10.8 | 9.9 | 156.3 | 134.1 | 14.2 | 9.8 | 8.4 |

[a] CTY= cobalt-time-yield (activity per total mass of cobalt).
[b] Relative loss of CTY (in %) from the initial (TOS→ 0) to the *pseudo*-steady state (SS).
[c] TOF= turnover frequency (activity per surface Co$^0$ sites as measured by H$_2$ chemisorption).

According to the characterizations discussed before, all three Co-Ru/TiO$_2$ catalysts display comparable Co$^0$ particle sizes of about 7-9 nm (based on STEM) and very high and alike degrees of cobalt reduction (ca. 90%). As mentioned in the introduction, a decrease in TOF for Co$^0$ nanoparticles sizing less than 6-8 nm has been reported for silica- and carbon-supported cobalt catalysts [3,4]. Although an equivalent particle size-TOF dependence has not yet been unambiguously demonstrated for TiO$_2$-supported cobalt catalysts, a significant impact of particle size on TOF for similarly-sized Co$^0$ particles in the 7-9 nm range, as for the present Co-Ru/TiO$_2$ catalysts, is not expected. Taking this into account, the fact that all catalysts display nearly the same initial TOF strongly suggests that the different extents of SMSI originated from the distinct support surface areas do not affect the initial intrinsic activity of the exposed metal cobalt sites. Differently, it can be seen in Table 5 that the TOF for Co-Ru/Ti-H in the *pseudo*-steady state (5.3·10$^{-2}$ s$^{-1}$) is about 1.6 times lower than the TOF for Co-Ru/Ti-M and Co-Ru/Ti-L (8.4·10$^{-2}$ s$^{-1}$). However, we have recently shown that the SMSI effect in Co-Ru/TiO$_2$ systems is partially reverted during the FTS reaction, likely due to water-assisted re-oxidation of the TiO$_x$ patches decorating the Co$^0$ nanoparticles, resulting in an increase in the amount of exposed Co$^0$ sites [19]. In consequence, the true concentration of active Co$^0$ sites in the Co-Ru/TiO$_2$ catalysts under FTS conditions is not known with certainty making the comparison of *pseudo*-steady state TOFs based on H$_2$ chemisorption data questionable. Therefore, a net influence of the extent of the SMSI decoration effect (directly

linked to the $TiO_2$ surface area) on the TOF of the exposed $Co^0$ centers in the *working* catalysts cannot be definitively concluded from our results. Nonetheless, large differences in TOF among the studied Co-Ru/$TiO_2$ catalysts during FTS reaction seem unlikely at the view of their almost identical initial TOF (at zero TOS) in spite of the notable differences in SMSI extent observed in their as-reduced state.

The selectivity to the different hydrocarbon fractions in the *pseudo*-steady state obtained for the Co-Ru/$TiO_2$ catalysts is compared in Table 6 at constant CO conversion (10 ± 1%). The selectivity to $CO_2$ was in all cases below 1%, as expected from the well known low activity of cobalt for the competing water gas shift reaction (WGSR). Results in Table 6 show no practical differences in the distribution of hydrocarbon products for the catalysts based on medium and low surface area $TiO_2$-anatase supports, both giving selectivities to methane ($C_1$) and liquids ($C_{5+}$) of ca. 12-13% and 74%, respectively. Comparatively, the catalyst supported on the high surface area $TiO_2$ displays higher selectivity to $C_1$ (16%) and lower to $C_{5+}$ (57%), implying that chain growth processes are inhibited in this catalyst experiencing the largest SMSI effect.

**Table 6.** Product distributions obtained in the *pseudo*-steady state on Co-Ru/$TiO_2$ catalysts at CO conversion of 10 ± 1%. Reaction conditions: T= 220 °C, P= 2.0 MPa, $H_2$/CO= 2 mol/mol, GHSV= 5.3 (for Co-Ru/Ti-H), 8.2 (for Co-Ru/Ti-M), and 11.0 (for Co-Ru/Ti-L) $L_{syngas}$/$g_{cat}$·h.

| Catalyst | Selectivity (%C) | | | Parameter $\chi^a$ |
|---|---|---|---|---|
| | $C_1$ | $C_2$-$C_4$ | $C_{5+}$ | ($10^{-16}$ m) |
| Co-Ru/Ti-H | 16.0 | 27.2 | 56.8 | 80 |
| Co-Ru/Ti-M | 12.2 | 13.9 | 73.9 | 97 |
| Co-Ru/Ti-L | 12.8 | 13.3 | 73.9 | 159 |

[a] Structural parameter modeling mass transport limitations in cobalt-catalyzed FTS (see text).

At constant reaction conditions and identical support identity, the distribution of hydrocarbons in FTS is mainly determined by the size of the cobalt nanoparticles [3,4], with more extended metal surfaces prevailing in larger particles favoring chain growth and hence $C_{5+}$ selectivity, and by mass transport effects [17]. In our case, the relatively small differences in $Co^0$ particle size between the three investigated catalysts (ca. 8±1 nm) hardly explain, by themselves, the significantly lower $C_{5+}$ selectivity (ca. 17% in absolute terms) displayed by

the high surface area Co-Ru/Ti-H catalyst. On the other hand, the crucial role played by mass transport limitations on the $C_{5+}$ selectivity of cobalt-based FTS catalysts under realistic conditions, particularly for catalyst pellet sizes commonly employed in fixed bed reactors, was highlighted several decades ago in the studies by Iglesia and co-workers [17,41]. According to the model developed by these authors, the $C_{5+}$ selectivity passes a maximum with increasing the severity of intraparticle diffusion resistance described by the structural parameter $\chi$ defined as in the following equation (1) [17]:

$$\chi = R_0^2 \cdot \varepsilon \cdot \theta_{Co}/r_p \qquad\qquad \text{Eq. (1)}$$

where $R_0$ is the mean radius of catalyst pellets, $\varepsilon$ is the pellet void fraction (porosity), $\theta_{Co}$ is the density of cobalt sites per unit area, and $r_p$ refers to the mean radius of the catalyst pores. According to this model [17], the $C_{5+}$ selectivity first raises with increasing diffusion limitations up to values of the structural parameter $\chi$ of around $170 \cdot 10^{16}$ m as re-adsorption of $\alpha$-olefins on the active sites and their participation in new chain growth processes become increasingly favored. Above this value of $\chi$ (that is, under more severe mass transport restrictions), a further increase of the structural parameter does not longer change the probability for $\alpha$-olefin re-adsorption and, instead, the resistance to the transport of CO through the liquid phase filling the pores becomes the limiting factor leading to a gradual decline of the $C_{5+}$ selectivity as $\chi$ increases.

In our case, the $\chi$ values calculated for the Co-Ru/TiO$_2$ catalysts fall in the range of $80 \cdot 10^{16}$-$160 \cdot 10^{16}$ m (Table 6) where $C_{5+}$ selectivity is mostly driven by the resistance to the diffusion of $\alpha$-olefins [17]. Interestingly, the parameter $\chi$ increases in the order: Co-Ru/Ti-H < Co-Ru/Ti-M << Co-Ru/Ti-L that is, with decreasing the support surface area or, equivalently, with increasing the average pore diameter. This trend looks at first sight surprising as a more restricted diffusion could be expected, *a priori*, for catalysts with smaller pores. However, taking into account that the radius of pellets ($R_0$) used in the catalytic experiments is the same for all three catalysts and that the mean catalyst pore radius ($r_p$) in the denominator of Eq. (1) varies only in a relatively short range (3.2-3.9 nm), it comes that the density of surface active Co$^0$ sites per unit area, given by the term $\theta_{Co}$ in eq. (1), is the most determinant factor influencing the final values of the parameter $\chi$ in our catalysts. In fact,

the trend for $\theta_{Co}$ is the same as that of $\chi$, increasing from Co-Ru/Ti-H ($1.88\cdot10^{17}$ at-Co$^0$/m$^2$) to Co-Ru/Ti-M ($2.58\cdot10^{17}$ at-Co$^0$/m$^2$) and further to Co-Ru/Ti-L ($6.56\cdot10^{17}$ at-Co$^0$/m$^2$). The significantly higher value of $\theta_{Co}$ (and of $\chi$) obtained for the low surface area Co-Ru/Ti-L sample originates from its higher concentration of surface Co$^0$ sites (due to the lower SMSI effect in this catalyst) and its lower specific surface area, as discussed previously on the basis of H$_2$ chemisorption and N$_2$ adsorption results. The increasing $\alpha$-olefin diffusion resistance with decreasing the surface area of the TiO$_2$-anatase support inferred from the calculated $\chi$ values is fully consistent with the variations in the olefin-to-paraffin (O/P) ratio of the produced hydrocarbons. In fact, as observed in Fig. 11, the O/P ratio for C$_2$-C$_4$ and C$_5$-C$_8$ hydrocarbons exhibits a decreasing trend with the parameter $\chi$ that reflects an increasing probability for $\alpha$-olefins to undergo secondary reactions such as re-adsorption and hydrogenation as their transport within the catalyst pellets becomes more impeded. In turn, the lower O/P ratio obtained for C$_5$-C$_8$ in comparison to C$_2$-C$_4$ could be anticipated considering the higher resistance to the diffusion of longer chain $\alpha$-olefins [17]. It is also worth of noting from the data in Fig. 11 that the O/P ratio for the C$_5$-C$_8$ fraction diminishes more rapidly with increasing $\chi$ than that of C$_2$-C$_4$ (for instance, the C$_2$-C$_4$-to-C$_5$-C$_8$ O/P ratio amounts to 1.3 for Co-Ru/Ti-H and 1.6 for Co-Ru/Ti-L), indicating that differences in diffusion resistance between the catalysts become more pronounced with increasing the chain length of the $\alpha$-olefin product.
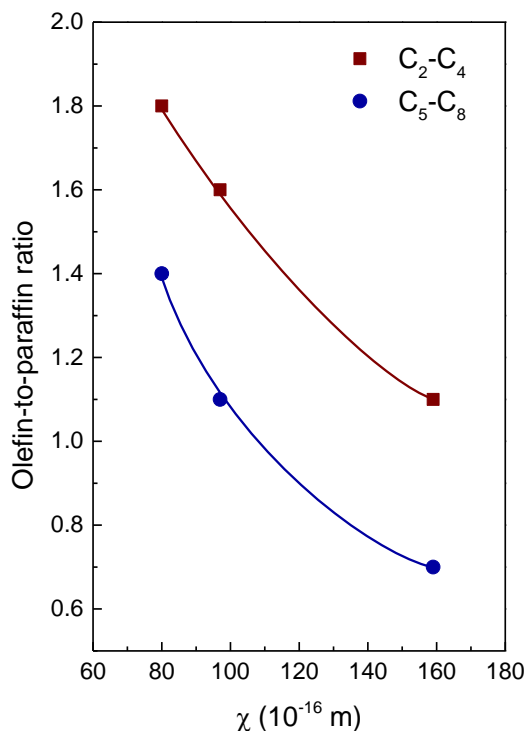
**Fig. 11.** Change in olefin-to-paraffin ratio for the $C_2$-$C_4$ and $C_5$-$C_8$ hydrocarbon fractions as a function of the diffusion-related structural parameter $\chi$.

Nonetheless, even though the hydrocarbon selectivities and O/P ratios follow the general trends expected from the values of the parameter $\chi$, the remarkably lower $C_{5+}$ selectivity observed for Co-Ru/Ti-H relative to the other two catalysts (Table 6) can hardly be accounted for by considering only mass transport issues. It is known from preceding surface science studies on model catalysts and theoretical calculations that CO dissociation and chain growth in FTS have distinct site requirements on cobalt catalysts [42]. Thus, while dissociation of CO is found to proceed readily on defected sites such as step edge sites on the surface of cobalt particles, chain growth involves rather large ensembles of $Co^0$ atoms on closed-packed terraces. Decoration of cobalt nanoparticles by the $TiO_x$ overlayer should expectedly decrease the size of the $Co^0$ ensembles and, consequently, disfavor chain growth (e.g. C-C bond formation) processes. Therefore, a smaller size for the chain growth ensembles could be envisaged for the Co-Ru/Ti-H sample exhibiting the most pronounced SMSI effect which, besides a lower resistance to the diffusion of $\alpha$-olefins as discussed before, would contribute to the much lower $C_{5+}$ selectivity of this catalyst.

Overall, the results presented in this study point towards a significant influence of the extent of SMSI, determined by the support surface area in the studied Co-Ru/TiO$_2$-anatase catalysts, on the cobalt-time-yield (without affecting initial TOFs) as well as on the hydrocarbon selectivity by modifying, respectively, the density of surface active Co$^0$ sites and the size of the ensembles where chain growth events preferentially take place.

## 4. Conclusions

TiO$_2$-anatase materials with specific surface areas of 53 (Ti-L), 117 (Ti-M), and 148 (Ti-H) m$^2$/g were hydrothermally synthesized by adjusting the conditions of the hydrothermal and/or calcination treatments, and applied as supports for preparing Co-Ru/TiO$_2$ catalysts (nominal loadings of 10 wt% Co and 0.5 wt% Ru) for Fischer-Tropsch synthesis (FTS). The specific surface area of the TiO$_2$ support was shown to influence the extent of the SMSI effect in the Co-Ru/TiO$_2$ catalysts after their reduction in H$_2$ at 400°C for 10 h. As-reduced catalysts displayed equivalent Co$^0$ particle sizes (7-9 nm) as determined by direct imaging (STEM) and degrees of cobalt reduction (about 90%), thus discarding any significant impact of these parameters on the observed catalytic performances. Lower H$_2$ uptakes, translating into larger relative differences between the Co$^0$ particle sizes measured by H$_2$ chemisorption and electron microscopy (STEM), and lower intensities of the cobalt-carbonyl bands in IR-CO surface titration experiments unambiguously evidenced a more pronounced SMSI decoration effect for catalysts prepared from higher surface area TiO$_2$ supports. This behavior can be related to a higher concentration of structural defects (i.e. Ti$^{3+}$/oxygen vacancy) in the high surface area TiO$_2$ samples comprising small crystallites, as supported by Raman spectroscopy, that results in the formation of more partially reduced TiO$_x$ species involved in the generation of the SMSI state during the H$_2$ reduction treatment. In consequence, the cobalt-time-yield (activity per total mass of cobalt) progressively decreased with the increase in TiO$_2$ surface area. Different extents of SMSI, however, did not apparently affect the initial activity of the catalysts per exposed Co$^0$ site as all three catalysts exhibited analogous initial TOFs ($10\pm1\cdot10^{-2}$ s$^{-1}$). On the other hand, a definitive conclusion on possible differences in TOF in the *pseudo*-steady state could not reached due to the partial reversibility of the SMSI effect that hampers an accurate determination of the concentration of surface Co$^0$ sites in the *working* catalysts. The Co-Ru/Ti-H catalyst, which experienced the largest SMSI extent, did also show the lowest selectivity to the desired liquid (C$_{5+}$) fraction.

Thus, at constant CO conversion of about 10%, the $C_{5+}$ selectivity was ~57% for Co-Ru/Ti-H and ~74% for both Co-Ru/Ti-M and Co-Ru/Ti-L. Such significantly lower $C_{5+}$ selectivity of Co-Ru/Ti-H was accounted for by considering the combined action of two effects, both having a negative impact on the chain growth probability: on one hand, a lower extent of $\alpha$-olefin re-adsorption and insertion into the growing chains, as inferred from the values of the structural parameter $\chi$, and on the other hand, to a greater reduction in the size of the $Co^0$ ensembles on the terraces of the nanoparticles (on which chain growth are believed to occur) due to the larger SMSI extent experienced by the catalyst supported on the high surface area $TiO_2$-anatase. In conclusion, we have shown in this work that the surface area of the $TiO_2$ carrier influences the extent of the SMSI effect in Co-Ru/$TiO_2$ catalysts and that this has a direct impact on both the activity and selectivity for the FTS reaction.

**Acknowledgments**

**References**

[1] M.E. Dry, J. Chem. Technol. Biotechnol. 77 (2002) 43–50.

[2] A.Y. Khodakov, W. Chu, P. Fongarland, Chem. Rev. 107 (2007) 1692–1744.

[3] G.L. Bezemer, J.H. Bitter, H.P.C.E. Kuipers, H. Oosterbeek, J.E. Holewijn, X. Xu, F. Kapteijn, A. J. Van Dillen, K.P. de Jong, J. Am. Chem. Soc. 128 (2006) 3956–3964.

[4] G. Prieto, A. Martínez, P. Concepción, R. Moreno-Tost, J. Catal. 266 (2009) 129–144.

[5] T.O. Eschemann, J.H. Bitter, K.P. de Jong, Catal. Today 228 (2014) 89–95.

[6] A. Martínez, G. Prieto, J. Rollán, J. Catal. 263 (2009) 292–305.

[7] G. Prieto, M.I.S. De Mello, P. Concepción, R. Murciano, S.B.C. Pergher, A. Martínez, ACS Catal. 5 (2015) 3323–3335.

[8] C. Liu, Y. Zhang, Y. Zhao, L. Wei, J. Hong, L. Wang, S. Chen, G. Wang, J. Li, Nanoscale 9 (2017) 570–581.

[9] T.O. Eschemann, J. Oenema, K.P. De Jong, Catal. Today 261 (2016) 60–66.

[10] G.L. Bezemer, P.B. Radstake, U. Falke, H. Oosterbeek, H.P.C.E. Kuipers, A.J. Van Dillen, K.P. De Jong, J. Catal. 237 (2006) 152–161.

[11] K. Shimura, T. Miyazawa, T. Hanaoka, S. Hirata, Appl. Catal. A Gen. 494 (2015) 1–11.

[12] G.R. Johnson, A.T. Bell, ACS Catal. 6 (2016) 100–114.

[13] G. Prieto, P. Concepción, R. Murciano, A. Martínez, J. Catal. 302 (2013) 37–48.

[14] J.A. Delgado, C. Claver, S. Castillón, D. Curulla-Ferré, V. V. Ordomsky, C. Godard, Appl. Catal. A Gen. 513 (2016) 39–46.

[15] J.Y. Park, Y.J. Lee, P.R. Karandikar, K.W. Jun, K.S. Ha, H.G. Park, Appl. Catal. A Gen. 411–412 (2012) 15–23.

[16] O. Borg, P.D.C. Dietzel, A.I. Spjelkavik, E.Z. Tveten, J.C. Walmsley, S. Diplas, S. Eri, A. Holmen, E. Rytter, J. Catal. 259 (2008) 161–164.

[17] E. Iglesia, Appl. Catal. A Gen. 161 (1997) 59–78.

[18] R.C. Reuel, C.H. Bartholomew, J. Catal. 85 (1984) 78–88.

[19] F. Bertella, P. Concepción, A. Martínez, Catal. Today (2016), http://dx.doi.org/10.1016/j.cattod.2016.08.008.

[20] A.M. Abdel-Mageed, D. Widmann, S.E. Olesen, I. Chorkendorff, J. Biskupek, R.J. Behm, ACS Catal. 5 (2015) 6753–6763.

[21] M. Bonne, P. Samoila, T. Ekou, C. Especel, F. Epron, P. Marécot, S. Royer, D. Duprez, Catal. Commun. 12 (2010) 86-91.

[22] M. Wu, G. Lin, D. Chen, G. Wang, D. He, S. Feng, R. Xu, Chem. Mater. 14 (2002) 1974–1980.

[23] D. Zhang, L. Qi, J. Ma, H. Cheng, J. Mater. Chem. 12 (2002) 3677–3680.

[24] C. Sanchez, J. Livage, M. Henry, F. Babonneau, J. Non. Cryst. Solids 100 (1988) 65–76.

[25] M. Thommes, K. Kaneko, A. V. Neimark, J.P. Olivier, F. Rodriguez-Reinoso, J. Rouquerol, K.S.W. Sing, Pure Appl. Chem. 87 (2015) 1051–1069.

[26] Y. Yue, Z. Gao, Chem. Commun. (2000) 1755–1756.

[27] H. Luo, C. Wang, Y. Yan, Chem. Mater. 15 (2003) 3841–3846.

[28] J. Hong, E. Marceau, A.Y. Khodakov, L. Gaberová, A. Griboval-Constant, J.S. Girardon, C. La Fontaine, V. Briois, ACS Catal. 5 (2015) 1273–1282.

[29] J. Li, G. Jacobs, Y. Zhang, T. Das, B.H. Davis, Appl. Catal. A Gen. 223 (2002) 195–203.

[30] J.A. Delgado, C. Claver, S. Castillón, D. Curulla-Ferré, V. V. Ordomsky, C. Godard, Appl. Catal. A Gen. 513 (2016) 39–46.

[31] Q. Cai, J. Li, Catal. Commun. 9 (2008) 2003–2006.

[32] S.J. Tauster, Acc. Chem. Res. 20 (1987) 389–394.

[33] D. Song, J. Li, Q. Cai, J. Phys. Chem. C 111 (2007) 18970–18979.

[34] G.L. Haller, D.E. Resasco, Adv. Catal. 36 (1989) 173-235.

[35] S.J. Tauster, S.C. Fung, J. Catal. 55 (1978) 29-35.

[36] J. Zheng, L. Liu, G. Ji, Q. Yang, L. Zheng, J. Zhang, ACS Appl. Mater. Interfaces 8 (2016) 20074-20081.

[37] Z. Xu, J. Shang, C. Liu, C. Kang, H. Guo, Y. Du, Mater. Sci. Eng. B 56 (1999) 211-214.

[38] T. Ohsaka, F. Izumi, Y. Fujiki, J. Raman Spectrosc. 7 (1978) 321-324.

[39] J.C. Parker, R.W. Siegel, Appl. Phys. Lett. 57 (1990) 943-945.

[40] T.O. Eschemann, K.P. de Jong, ACS Catal. 5 (2015) 3181–3188.

[41] E. Iglesia, S.L. Soled, J.E. Baumgartner, S.C. Reyes, J. Catal. 153 (1995) 108–122.

[42] C.J. Weststrate, P. van Helden, J.W. Niemantsverdriet, Catal. Today 275 (2016) 100–110.